



# Relationship between catalytic deactivation and physicochemical properties of $\text{LaMnO}_3$ perovskite catalyst during catalytic oxidation of vinyl chloride

Chuanhui Zhang<sup>a,b,1</sup>, Chao Wang<sup>a,b,1</sup>, Wenchao Hua<sup>a</sup>, Yanglong Guo<sup>a,\*</sup>, Guanzhong Lu<sup>a</sup>, Sonia Gil<sup>b</sup>, Anne Giroir-Fendler<sup>b,\*\*</sup>

<sup>a</sup> Key Laboratory for Advanced Materials and Research Institute of Industrial Catalysis, East China University of Science and Technology, Shanghai 200237, PR China

<sup>b</sup> Université Lyon 1, CNRS, UMR 5256, IRCÉLYON, Institut de Recherches sur la Catalyse et l'Environnement de Lyon, 2 Avenue Albert Einstein, 69626 Villeurbanne Cedex, France

## ARTICLE INFO

### Article history:

Received 28 September 2015

Received in revised form

22 December 2015

Accepted 31 December 2015

Available online 6 January 2016

### Keywords:

Deactivation

Vinyl chloride

$\text{LaMnO}_3$

Perovskite

Physicochemical property

## ABSTRACT

A  $\text{LaMnO}_3$  perovskite oxide catalyst prepared by co-precipitation was evaluated for vinyl chloride (VC) oxidation over consecutive catalytic cycles and in steady-state conditions. The  $\text{LaMnO}_3$  catalyst exhibited relatively poor catalytic stability and durability, with the amount of chlorinated organic species increasing as catalytic activity decreased. Physicochemical properties were characterized by X-ray diffraction (XRD),  $\text{N}_2$  sorption, thermogravimetric and differential thermal analysis (TGA/DTA), energy dispersive spectroscopy (EDS), hydrogen temperature-programmed reduction ( $\text{H}_2$ -TPR), oxygen temperature-programmed desorption ( $\text{O}_2$ -TPD) and X-ray photoelectron spectroscopy (XPS). Fresh and used catalysts presented a typical perovskite structure. No coke and only traces of residual chlorine species were detected on the used catalyst, indicating that coke formation and attack by chlorine were not the causes for deactivation. The used catalyst, however, presented lower specific surface area, low-temperature reducibility and surface oxygen mobility than the fresh one, suggesting that physicochemical and redox properties strongly influenced catalytic deactivation. Finally, a deactivation mechanism was proposed based on the  $\text{Mn}^{4+}/\text{Mn}^{3+}$  redox cycle, and the formation of chlorinated by-products was inferred to be closely related to the presence of Cl species and catalyst deactivation.

© 2016 Published by Elsevier B.V.

## 1. Introduction

As one of the major contributors to atmospheric pollution, chlorinated volatile organic compounds (CVOCs) are heavily emitted in numerous domains including manufacturing production, engine exhaust, construction and laundry or printing works. For instance, large quantities of vinyl chloride (VC) emissions with a concentration of up to 1–2% are released in the industrial process for polyvinyl chloride (PVC) production, resulting in tangible environmental damage and detrimental effects on human health. Due to the environmentally unfriendly and carcinogenic properties of these compounds, major entities such as the European

Communities and the United Nations have enacted stringent environmental regulations to limit atmospheric emissions of CVOCs [1,2].

Among the technologies used for CVOCs abatement, catalytic oxidation is recognized as the most promising one for eliminating such hazardous, toxic compounds. Within this pathway, CVOCs can be completely oxidized into carbon dioxide ( $\text{CO}_2$ ), water ( $\text{H}_2\text{O}$ ) and hydrochloric acid (HCl) at relatively low temperature. Furthermore, the final products of CVOCs oxidation are environmentally friendly, provided that an easy procedure is put into place to neutralize hazardous and corrosive hydrochloric acid using a concentrated alkali solution, and thereby no secondary pollution occurs throughout the abatement process.

Most of the recent studies of catalysts for the catalytic oxidation of CVOCs have focused on solids in three categories, namely supported precious metals (e.g.,  $\text{Pt}/\text{Al}_2\text{O}_3$  and  $\text{Pd}/\text{Al}_2\text{O}_3$ ) [3,4], zeolites (e.g., H-Y, H-MOR and H-ZSM-5) [5,6] and transition metal oxides (e.g.,  $\text{CeO}_2$ ,  $\text{MnO}_x$  and  $\text{Co}_3\text{O}_4$ ) [7,8]. It is well accepted that pre-

\* Corresponding author. Tel.: +86 21 64 25 29 23; fax: +86 21 64 25 29 23.

\*\* Corresponding author. Tel.: +33 4 72 43 15 86; fax: +33 4 72 43 16 95.

E-mail addresses: [ylguo@ecust.edu.cn](mailto:ylguo@ecust.edu.cn) (Y. Guo),

[anne.giroir-fendler@ircelyon.univ-lyon1.fr](mailto:anne.giroir-fendler@ircelyon.univ-lyon1.fr) (A. Giroir-Fendler).

<sup>1</sup> These authors contributed equally to this work as co-first authors.

cious metals exhibit excellent catalytic activity for CVOs oxidation. Nonetheless, their high cost, low thermal stability and susceptibility to poisoning are important problems that remain to be resolved. Zeolites, which are inexpensive catalytic materials with high specific surface areas and variable pore structures, present good catalytic performance for CVOs oxidation, and their promising activities have been closely related to the remarkable acidic properties of these materials [6,9]. Coke deposition and chlorine adsorption nevertheless tend to occur on the acid sites of zeolites, leading to rapid deactivation as well as structural changes [10,11].

Meanwhile, transition metal oxides are currently attracting much attention as a promising alternative for CVOs abatement because of their low cost, relatively high catalytic activity and favorable resistance toward chlorine poisoning. Recently, Dai et al. [12] reported that MnCeLa mixed oxides showed high activity, good selectivity and desirable stability for the catalytic oxidation of chlorobenzene (CB). The promising stability of this catalyst could be attributed to the high mobility of oxygen on the interface between the  $\text{MnCeO}_x$  solid solution and  $\text{MnO}_x$ , which is critical for removing the Cl species produced during CB decomposition. Ce-Pr mixed oxides, specifically  $\text{Ce}_{0.5}\text{Pr}_{0.5}\text{O}_2$ , have been reported to exhibit superior stability for the catalytic combustion of 1,2-dichloroethane [13]. No apparent deactivation was observed for this catalyst following three consecutive catalytic cycles from 150 to 500 °C and a durability test at 335 °C for 115 h.

Among transition metal oxides,  $\text{LaMnO}_3$  perovskite oxide has been studied as a CVOs oxidation catalyst since the early 1990s by Wendt et al. [14,15] and Siquin et al. [16,17]. It has been shown that numerous C1 ( $\text{CH}_3\text{Cl}$ ,  $\text{CH}_2\text{Cl}_2$ ,  $\text{CHCl}_3$  and  $\text{CCl}_4$ ) and C2 ( $\text{CCl}_3\text{CH}_3$ ,  $\text{CH}_2\text{ClCH}_2\text{Cl}$ ) chlorohydrocarbons can be completely decomposed over  $\text{LaMnO}_3$  catalysts at relatively low temperature (below 550 °C). Conspicuous catalytic deactivation was, however, induced through the formation of by-products such as C–C coupling products, higher chlorinated compounds and cracking compounds. In our previous works [18,19], a  $\text{LaMnO}_3$  perovskite oxide catalyst synthesized by co-precipitation was found to exhibit significant activity for the catalytic oxidation of VC emissions. Moreover, its activity was enhanced by A- or B-site substitution. Because a promising catalyst for industrial applications should present not only high catalytic activity, but also good stability and durability, further study relative to stability and deactivation issues for  $\text{LaMnO}_3$  is now of the utmost urgency and significance.

In this work, a  $\text{LaMnO}_3$  perovskite oxide prepared by co-precipitation was subjected to catalytic stability testing in consecutive light-off experiments and to a steady-state durability evaluation (120 h) for VC oxidation. Various characterization techniques including XRD,  $\text{N}_2$  sorption, TG/DTA, EDS,  $\text{H}_2$ -TPR, XPS and  $\text{O}_2$ -TPD were used to investigate the physicochemical properties of fresh and used catalysts. Finally, a deactivation mechanism was proposed on the basis of these characterization results.

## 2. Experimental

### 2.1. Catalyst preparation

$\text{LaMnO}_3$  perovskite oxide was prepared by conventional co-precipitation using a mixed aqueous solution of  $\text{NaOH}$  ( $2 \text{ mol L}^{-1}$ ) and  $\text{Na}_2\text{CO}_3$  ( $1 \text{ mol L}^{-1}$ ), as the precipitating agent. Equimolar amounts of lanthanum and manganese nitrates serving as precursors were dissolved in 25 mL of distilled water to yield a mixed aqueous solution. Subsequently, the  $\text{NaOH}$ – $\text{Na}_2\text{CO}_3$  aqueous solution was added dropwise to the previous solution under magnetic stirring until the pH value reached 10. After the resulting suspension was aged for 4 h at room temperature, the precipitate was filtered and thoroughly washed with distilled water, then dried at

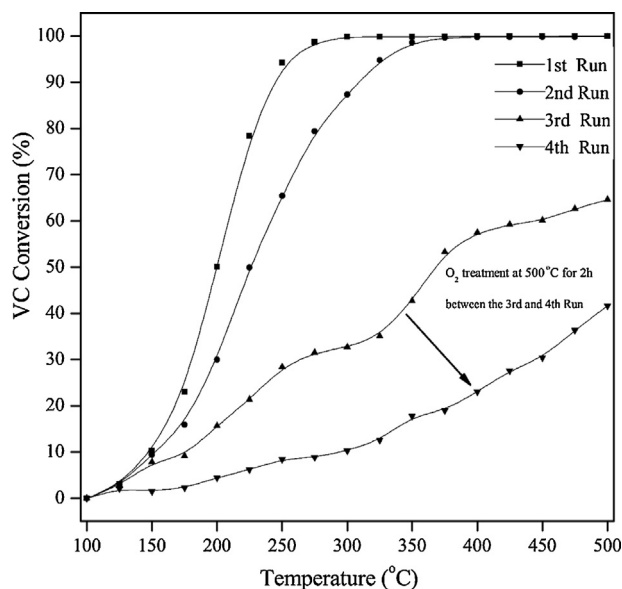


Fig. 1. VC conversion as a function of reaction temperature over  $\text{LaMnO}_3$  catalyst in a four-run catalytic test (VC concentration: 1000 ppm; GHSV: 15 000  $\text{h}^{-1}$ ).

120 °C overnight and calcined at 750 °C (heating rate 5 °C  $\text{min}^{-1}$ ) for 2 h, yielding the perovskite structure.

### 2.2. Catalyst characterizations

Powder X-ray diffraction (XRD) patterns were recorded on a Bruker D8 Focus diffractometer using  $\text{Cu K}\alpha$  radiation ( $\lambda = 1.5406 \text{ \AA}$ , operated at 40 kV and 40 mA with a scanning rate of 6°  $\text{min}^{-1}$ ) in the  $2\theta$  range of 20–80°. Phase identification was performed by referring to the standard powder diffraction file (PDF) in the database of the International Center of Diffraction Data (ICDD).

Nitrogen sorption at 77 K was performed on a Micromeritics ASAP 2020 M surface area and porosity analyzer. Before the measurement, the catalysts were degassed at 300 °C for 6 h to remove moisture and impurities. The Brunauer–Emmett–Teller (BET) method was used to calculate the specific surface area (SSA) of each catalyst.

Elemental chemical compositions of all catalysts were analyzed using an EDAX Falcon energy dispersive spectrometer (EDS) built into a JSM-6360LV scanning electron microscope.

Thermo-gravimetric/differential thermal analysis (TG/DTA) was performed on a PerkinElmer Pyris Diamond with a WCT-2 thermal analyzer at a heating rate of 10 °C  $\text{min}^{-1}$  from room temperature to 800 °C under air atmosphere.

Hydrogen temperature-programmed reduction ( $\text{H}_2$ -TPR) was carried out on a Micromeritics AutoChem11 2920 sorption instrument equipped with a thermal conductivity detector (TCD). Prior to the experiment, 100 mg of the catalyst was pretreated in a 3 vol.%  $\text{O}_2/\text{He}$  stream at 500 °C for 30 min in order to achieve complete oxidation. After cooling to room temperature, a 5 vol.%  $\text{H}_2/\text{Ar}$  gas mixture with a flow rate of 50  $\text{mL min}^{-1}$  was introduced, and the reactor was heated at a rate of 10 °C  $\text{min}^{-1}$  from room temperature to 900 °C and maintained at this temperature for 20 min. The TCD response was calibrated with an  $\text{Ag}_2\text{O}$  sample (provided by Micromeritics Co., Ltd.) as a standard.

X-ray photoelectron spectroscopy (XPS) were conducted on a ThermoESCALAB250 spectrometer with a monochromatized  $\text{Al K}\alpha$  X-ray source (1486.6 eV) and a passing energy of 20 eV. The binding energy (BE) was determined by utilizing C1s of adventitious carbon (284.8 eV) as a reference. The XPS spectra were deconvoluted

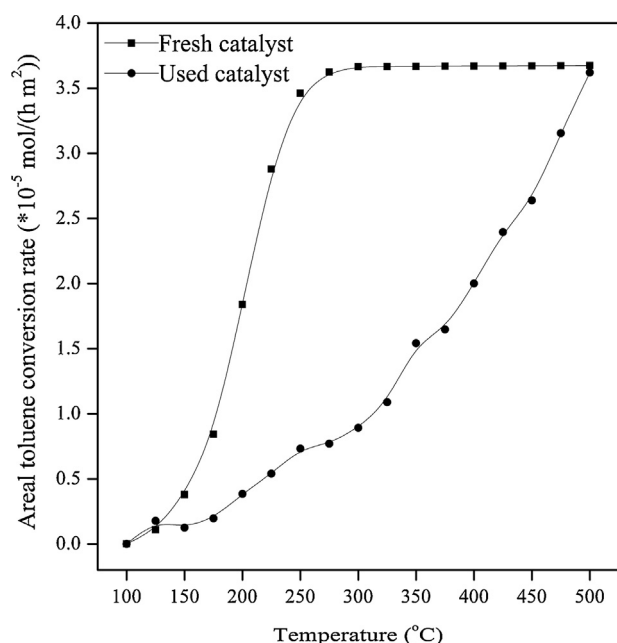


Fig. 2. Areal toluene conversion rate as a function of reaction temperature in the 1st run (fresh catalyst) and the 4th run (used catalyst).

using the XPSPEAK 41 program by curve fitting after Shirley-type background subtraction.

Oxygen temperature-programmed desorption (O<sub>2</sub>-TPD) experiments were also conducted on the Micromeritics AutoChem11 2920 sorption instrument, and the desorption signal of oxygen was recorded by an online Hiden Analytical HAL301 mass spectrometer (MS). Prior to testing, 100 mg of the catalyst was pretreated in a 3 vol.% O<sub>2</sub>/He gas mixture at 550 °C for 60 min. After cooling to room temperature under this atmosphere, a stream of pure He with a flow rate of 30 mL min<sup>-1</sup> purged the reactor until the stabilization of MS baseline. The reactor was then heated at a rate of 15 °C min<sup>-1</sup> from room temperature to 900 °C. Simultaneously, the signal of desorbed oxygen was collected by the MS detector.

### 2.3. Catalytic activity and durability evaluation

Catalytic tests were performed in a quartz tubular (I.D. = 12 mm) fixed-bed reactor operated at atmospheric pressure. Typically, 0.5 g of the catalyst (40–60 mesh) was packed into the reactor with the load volume of 0.48 mL and the height of 10 mm, and evaluated for its activity in the 50–500 °C temperature range. The reaction temperature was monitored by a thermocouple placed in the middle of the catalyst bed. Liquefied VC (b.p. = −13.9 °C), stored in a stainless-steel cylinder, was gasified at room temperature (25 °C). The gaseous VC, controlled by a digital mass flowmeter (SeverStar) and set with a flow rate of 0.12 mL min<sup>-1</sup>, was diluted with air to reach a VC concentration of 1000 ppm. The total flow rate was 120 mL min<sup>-1</sup>, corresponding to a gas hourly space velocity (GHSV) of 15,000 h<sup>-1</sup>. The VC and organic by-products in the effluent gas was analyzed by an online PerkinElmer Clarus 580 gas chromatograph equipped with a flame ionization detector (FID). In addition, a PerkinElmer TurboMatrix 650 thermal desorber combined with an Agilent 5975C inert mass spectrum equipped with a triple-Axis detector was used for the trapping and qualitative determination of the possible chlorinated intermediates, namely chloroform (CHCl<sub>3</sub>), carbon tetrachloride (CCl<sub>4</sub>) and trichloroethane (CH<sub>2</sub>ClCHCl<sub>2</sub>), and their concentrations were quantitatively determined by an external standard method. Preliminary

Table 1

Temperatures at 10, 50 and 90% of VC conversion over LaMnO<sub>3</sub> catalyst in each catalytic run (O<sub>2</sub> treatment at 500 °C for 2 h between Run 3 and 4).

Run	Temperature (°C) <sup>a</sup>		
	<i>T</i> <sub>10</sub>	<i>T</i> <sub>50</sub>	<i>T</i> <sub>90</sub>
1st run	146	199	243
2nd run	152	225	307
3rd run	175	367	–
4th run	290	–	–

<sup>a</sup> Light-off temperatures at 10, 50 and 90% of VC conversion, respectively.

experiments ruled out the existence of heat/mass transport limitations.

The durability of the LaMnO<sub>3</sub> catalyst was evaluated under the same reaction conditions with a VC concentration of 1000 ppm and a GHSV of 15,000 h<sup>-1</sup>. Catalytic testing of VC oxidation was continuously performed at 350 °C for 120 h, and the corresponding VC conversion and products distribution were analyzed using samples taken at hourly intervals.

## 3. Results and discussion

### 3.1. Catalytic stability, durability and by-products distribution for VC oxidation

The catalytic stability of LaMnO<sub>3</sub> perovskite oxide was studied via four consecutive light-off tests. It should be noted that after the third run, the catalyst was pretreated in an oxygen atmosphere at 500 °C for 2 h before being subjected to the fourth run. The light-off curves of VC oxidation as a function of reaction temperature over LaMnO<sub>3</sub> catalyst are displayed in Fig. 1. *T*<sub>10</sub>, *T*<sub>50</sub> and *T*<sub>90</sub>, corresponding to the temperatures at 10%, 50% and 90% VC conversion, are summarized in Table 1.

The LaMnO<sub>3</sub> catalyst exhibited the highest catalytic activity for VC oxidation in the first run with *T*<sub>10</sub>, *T*<sub>50</sub> and *T*<sub>90</sub> values of 146, 199 and 243 °C, respectively. In the second run, the light-off curve shifted toward higher temperature, with *T*<sub>10</sub>, *T*<sub>50</sub> and *T*<sub>90</sub> reaching respective values of 152, 225 and 307 °C. In spite of this decreased catalytic activity in the second run, complete VC conversion was still achieved below 400 °C. Deactivation occurred to a greater extent in the third run, however, with *T*<sub>10</sub> and *T*<sub>50</sub> attaining 175 and 367 °C. Even at 500 °C, only 65% of the VC was converted.

After the third run, the deactivated catalyst was pretreated in an oxygen atmosphere at 500 °C for 2 h and reused for the fourth run. During the temperature-rise process of the pretreatment, an online Hiden HPR20 quadrupole mass spectrometer was used to record the desorption signals of adsorbates such as H<sub>2</sub>O, VC, Cl and CO<sub>2</sub> (further results in Section 3.2). Despite this reoxidation step, LaMnO<sub>3</sub> perovskite oxide exhibited lower catalytic activity than that in the previous cycles, with VC conversion increasing slowly as the rise of temperature. At 290 °C, only 10% of the VC was converted, whereas complete conversion was achieved in the first run at the same temperature. Even at 500 °C, VC conversion remained below 50%. Moreover, the areal toluene conversion rate (molar flow rate per unit area of the catalyst, mol h<sup>-1</sup> m<sup>-2</sup>) as a function of reaction temperature in the 1st run (fresh catalyst) and the 4th run (used catalyst) was determined and shown in Fig. 2. It can be observed that the used catalyst exhibited much lower areal toluene rate than the fresh one in the temperature range of 125–500 °C, which confirmed its catalytic deactivation.

These results suggest that the LaMnO<sub>3</sub> catalyst suffered from poor catalytic stability for VC oxidation, leading to irreversible deactivation closely related to the changes in physicochemical properties of the catalyst over the course of the reaction.

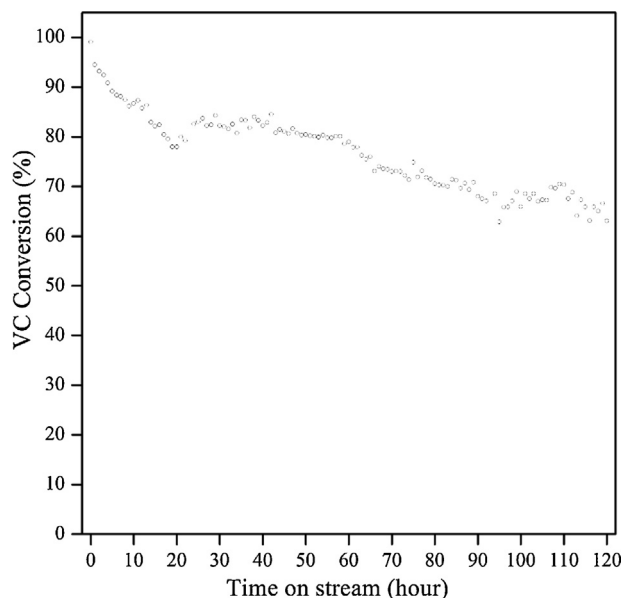


**Fig. 3.** VC conversion as a function of time on stream over  $\text{LaMnO}_3$  catalyst at  $350^\circ\text{C}$  (VC concentration: 1000 ppm; GHSV:  $15\,000\text{ h}^{-1}$ ).

Catalytic stability was evaluated under steady-state conditions at  $350^\circ\text{C}$  after the first run. Fig. 3 illustrates VC conversion as a function of time on stream over the  $\text{LaMnO}_3$  catalyst. It appears that  $\text{LaMnO}_3$  perovskite oxide was deactivated the most quickly during the first 20 h (from 100 to 78%), then more gradually until the end of the reaction (120 h), at which point 63% of VC conversion was noted.

The ideal products for complete oxidation of VC are  $\text{CO}_2$ ,  $\text{H}_2\text{O}$  and  $\text{HCl}$  without any formation of other chlorinated hydrocarbons, due to the VC dehydrochlorination at relatively low temperature, and the further thermal decomposition of hydrocarbons at high temperature. However, highly activated chlorine species will unavoidably undergo chlorination reactions with hydrocarbon intermediates due to the catalytic effect of  $\text{LaMnO}_3$  perovskite oxide. In addition to  $\text{H}_2\text{O}$  and  $\text{CO}_2$ , this results in the production of some higher chlorinated organic species.

The effluent gas from the steady-state test was analyzed by FID, where  $\text{CHCl}_3$ ,  $\text{CCl}_4$  and  $\text{CHCl}_2\text{CH}_2\text{Cl}$  were found as the organic by-products of VC oxidation. Fig. 4 shows the concentrations of organic by-products as a function of time on stream over  $\text{LaMnO}_3$  at  $350^\circ\text{C}$ . The concentrations of chlorinated hydrocarbons increased as the decrease in VC conversion (Fig. 3). Total VC conversion was observed at the beginning of the steady-state test, without any formation of chlorinated by-products. During the first 20 h, however, the concentrations of  $\text{CHCl}_3$ ,  $\text{CCl}_4$  and  $\text{CHCl}_2\text{CH}_2\text{Cl}$  continuously increased while VC conversion clearly decreased. This suggests that the formation of the chlorinated hydrocarbons was closely related to catalyst deactivation. Finally, the concentrations of  $\text{CCl}_4$  and  $\text{CHCl}_2\text{CH}_2\text{Cl}$  were relatively stable (around 10 and 3 ppm, respectively), while that of  $\text{CHCl}_3$  gradually increased (64 ppm at 120 h).

### 3.2. Catalyst characterizations

Several characterization techniques were performed over the fresh and used (after four consecutive light-off experiments in the temperature range of  $50$ – $500^\circ\text{C}$ ) catalysts in order to better understand the deactivation process. The physicochemical properties and elemental compositions of the fresh and used catalysts are summarized in Table 2.

XRD patterns of fresh and used catalysts are shown in Fig. 5. The characteristic diffraction peaks of the fresh catalyst corre-

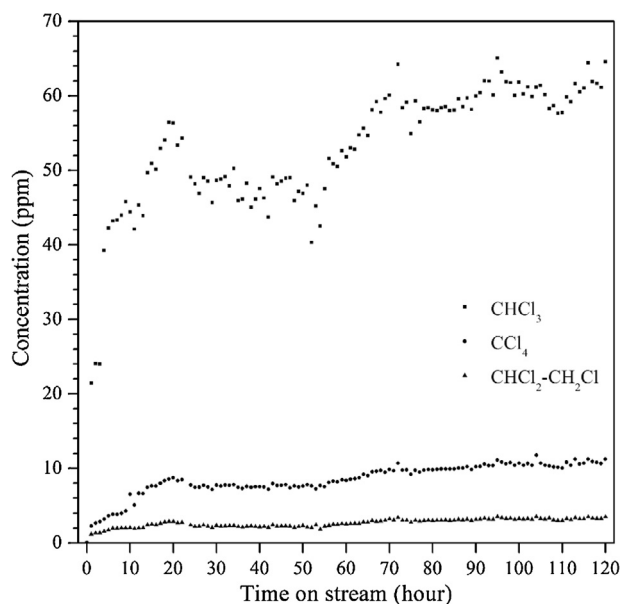


**Fig. 4.** Concentration of chlorinated by-products as a function of time on stream over  $\text{LaMnO}_3$  catalyst at  $350^\circ\text{C}$  (VC concentration: 1000 ppm; GHSV:  $15\,000\text{ h}^{-1}$ ).

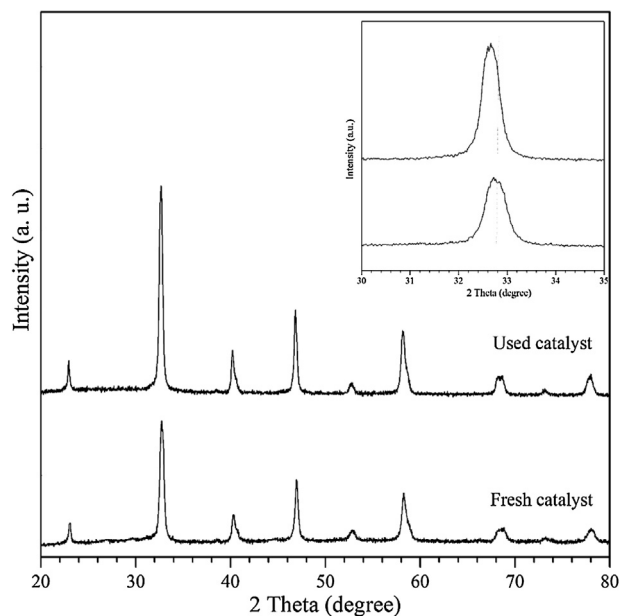


**Fig. 5.** XRD patterns of fresh and used catalysts.

lated well with those of the  $\text{LaMnO}_{3.26}$  (JCPDS PDF# 50-0299) perovskite structure, corresponding to a rhombohedral symmetry (space group  $R\bar{3}c$ ), in agreement with Alonso et al. [20] and He et al. [21]. Meanwhile, the used catalyst showed a typical  $\text{LaMnO}_{3.15}$  (JCPDS PDF# 50-0298) structure with the same symmetry as  $\text{LaMnO}_{3.26}$ .

Due to the detection limitations of the XRD measurements, it was difficult to observe the possible presence of other solid phases such as manganese oxide ( $\text{MnO}_x$ ) and/or lanthanum oxide ( $\text{La}_2\text{O}_3$ ) on either catalyst, indicating that well-formed, single-phase perovskite structures were obtained. The used catalyst, however, presented sharper diffraction peaks with higher peak intensity and narrower peak width than the fresh one, suggesting an enhancement of crystallinity after several catalytic runs. Additionally, a slight shift (about  $0.2^\circ$ ) toward lower Bragg angles was observed for the used catalyst, which could be attributed to lattice expan-



**Table 2**  
Physicochemical properties and elemental compositions of fresh and used catalysts.

Catalysts	Crystallite size <sup>a</sup> (nm)	Symmetry <sup>b</sup>	Unit-cell parameters <sup>b</sup>				SSA <sup>c</sup> (m <sup>2</sup> g <sup>-1</sup> )	Elemental compositions <sup>d</sup> (atomic ratio)				
			a (Å)	b (Å)	c (Å)	Vol (Å <sup>3</sup> )		La%	Mn%	O%	Na%	Cl%
Fresh	16.6	Rhombohedral R-3c	5.4884	5.4884	13.2865	346.6	17.5	27.25	27.09	42.03	3.63	–
Used	19.2	Rhombohedral R-3c	5.4973	5.4973	13.3620	349.7	7.4	26.53	27.41	42.91	3.16	–

<sup>a</sup> Calculated from line broadening of LaMnO<sub>3</sub> by Scherrer equation.

<sup>b</sup> Determined and calculated from the XRD patterns by MDI Jade 5.0 program.

<sup>c</sup> Measured from the N<sub>2</sub> sorption by BET method.

<sup>d</sup> Determined from EDS analysis.

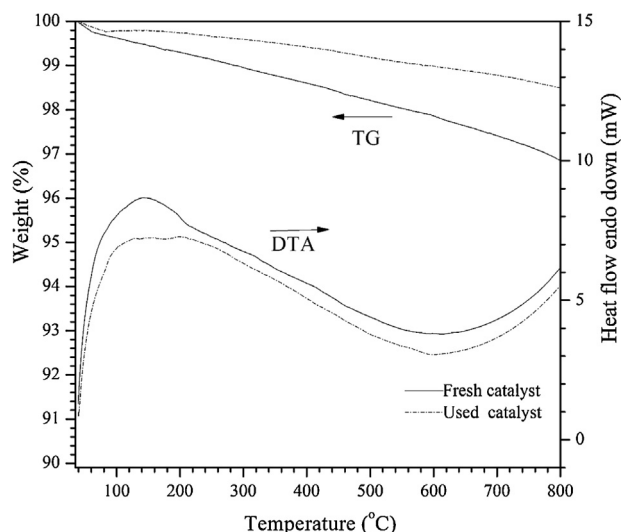


**Fig. 6.** TG/DTA curves of fresh and used catalysts.

sion and increased crystallite size. These results agree with the textural parameters presented in Table 2, in which the used catalyst presents a larger crystal size and higher unit-cell parameters (indicating crystal lattice expansion), compared to the fresh catalyst.

Moreover, the used catalyst exhibited a lower specific surface area (SSA) than its fresh counterpart (7.4 m<sup>2</sup> g<sup>-1</sup> and 17.5 m<sup>2</sup> g<sup>-1</sup>, respectively, Table 2), suggesting that this decrease in SSA could be an important factor for catalytic deactivation.

Within experimental error, the elemental compositions of the fresh and used LaMnO<sub>3</sub> oxides were fairly close. Due to the addition of NaOH–Na<sub>2</sub>CO<sub>3</sub> aqueous solution during catalyst preparation, a significant amount of residual sodium was still present on the catalysts despite thorough washing. Large amounts of chlorine produced from CVOCs decomposition can strongly adsorb on catalyst surfaces, blocking the active sites and even, in some situations, provoking chlorination reactions with metal oxides that alter chemical structures and components [13,22]. The amounts of residual chlorine were therefore determined, but they were negligible for both catalysts, with no result from EDS analysis (Cl% in Table 2), and no peaks assigned to Cl found in EDS spectra (shown in Fig. S1). This can be attributed to the presence of manganese-based oxide, which can effectively remove the Cl species from a catalytic surface [12,23]. Furthermore, no characteristic diffraction peaks assigned to LaCl<sub>3</sub>, LaOCl and/or MnCl<sub>x</sub> were detected in the XRD pattern of the used catalyst, suggesting that no chlorinated oxides were finally formed.

Coke formation is one of the main causes of deactivation in oxidation reactions [11,24]. Particularly, for the abatement of chlorinated hydrocarbons over protonic and metal-exchanged zeolites, coke formation is liable to occur on the acid sites [10,24]. Therefore, in order to investigate if coke was formed during testing, TG/DTA analysis was performed. As shown in Fig. 6, for the fresh catalyst,

a relatively small weight loss of ca. 3.3% was observed between 25 and 800 °C, with a broad endothermic peak at about 150 °C that can likely be attributed to the removal of chemisorbed and/or crystalline water on the catalyst. For the used catalyst, a smaller weight loss of ca. 1.6% was obtained with a similar endothermic peak. It can be assumed that, in addition to the removal of adsorbed and/or hydrated water, the desorption of traces of chlorinated species could contribute to the total weight loss. That said, the larger crystallite size and lower SSA of the used catalyst after its four continuous catalytic runs led to there being smaller amounts of adsorbates, which thereby induced a lower weight loss. From these results, it can be confirmed that no coke formation occurred on the LaMnO<sub>3</sub> catalyst in the total oxidation of VC.

Moreover, the desorption behaviors of possible adsorbed species including water (H<sub>2</sub>O, m/e = 18), VC (m/e = 27), chlorine (Cl, m/e = 35) and carbon dioxide (CO<sub>2</sub>, m/e = 44) were examined by an online mass spectrometer during the thermal pretreatment process after the third catalytic run, and the recorded signals are displayed in Fig. 7. An intense peak corresponding to H<sub>2</sub>O desorption can be observed at 150 °C (Fig. 7A), and a weak, broad peak centered at 150 °C can be assigned to Cl desorption (Fig. 7C). The temperature of these desorption peaks agrees with that of the endothermic peak visible in the DTA curve (Fig. 6). As seen from Fig. 7B and D, no obvious desorption signals corresponding to VC and CO<sub>2</sub> were detected, revealing that (i) adsorbed water and traces of residual chlorine were the main adsorbates on the catalyst, which resulted in a small weight loss; (ii) VC was not adsorbed on the catalyst; and (iii) coke was not present on the catalyst due to the absence of CO<sub>2</sub> desorption signal. All of these observations concur with the results of the TG–DTA analysis.

H<sub>2</sub>-TPR experiments were conducted to investigate the reducibility of the fresh and used catalysts, and the recorded profiles are illustrated in Fig. 8. For each catalyst, two reduction steps were obtained, one in a low-temperature range (50–500 °C) and the other in a high-temperature range (500–800 °C). It is well accepted that Mn<sup>2+</sup> is the final oxidation state in the reduction process of manganese oxides without the reduction of Mn<sup>2+</sup> into metallic manganese [25,26]. In addition, a considerable proportion of Mn<sup>4+</sup> could be present in LaMnO<sub>3</sub>-based perovskite oxides, which results in the presence of crystal defects and over-stoichiometric oxygen. Thus, the fresh LaMnO<sub>3</sub> catalyst presented two peaks centered at 263 and 698 °C, respectively. The first peak could be correlated with the reduction of Mn<sup>4+</sup> into Mn<sup>3+</sup> as well as with the removal of surface adsorbed oxygen species, whereas the second peak at high temperature could be attributed to the reduction of Mn<sup>3+</sup> into Mn<sup>2+</sup> [18]. The used catalyst, however, presented a smaller reduction peak at 289 °C and a broad shoulder near 415 °C in the low-temperature range corresponding to the reduction of Mn<sup>4+</sup> into Mn<sup>3+</sup>, with the overall reduction bands shifted toward higher temperature than for the fresh catalyst. Furthermore, the reduction of Mn<sup>4+</sup> into Mn<sup>3+</sup> was inhibited, which could be due to sintering and enhancement of crystallinity after consecutive catalytic tests. These results therefore indicate that the used LaMnO<sub>3</sub> perovskite exhibited lower reducibility than its fresh counterpart.

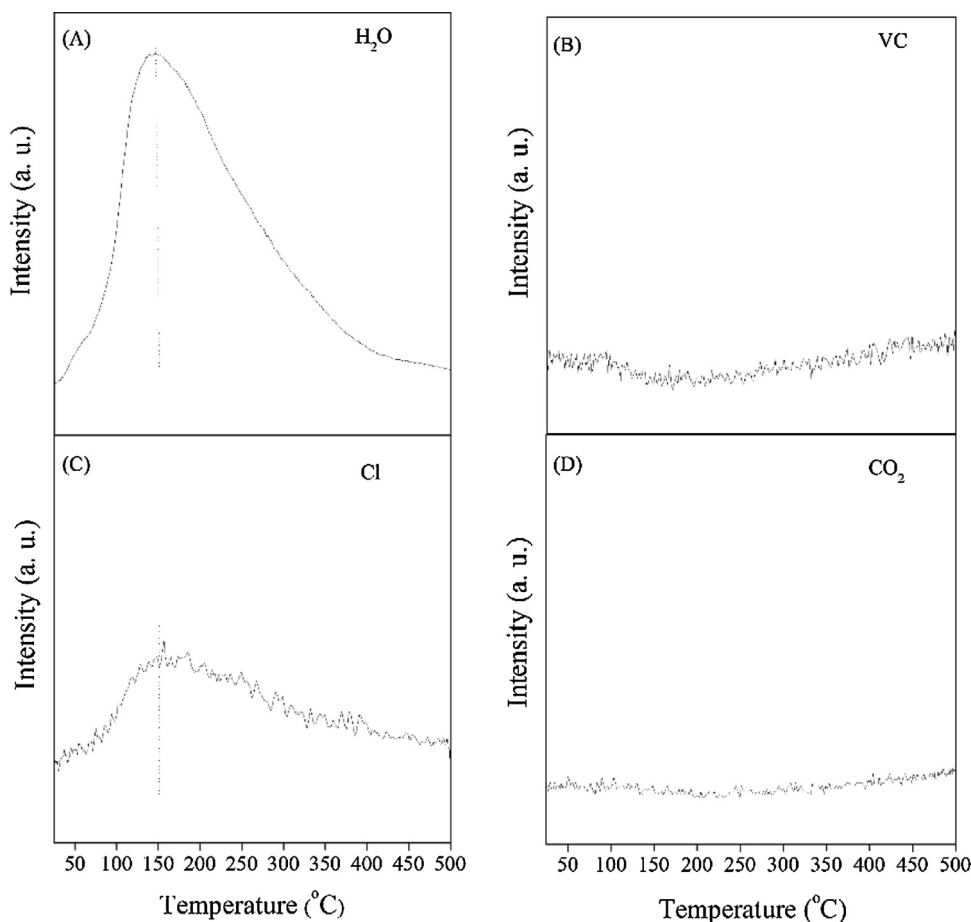


Fig. 7. Desorption signals of (A) H<sub>2</sub>O, (B) VC, (C) Cl and (D) CO<sub>2</sub> on the catalyst during thermal treatment under O<sub>2</sub> atmosphere.

**Table 3**  
H<sub>2</sub> consumption of fresh and used catalysts.

Catalysts	Low-temperature range				High-temperature range		Total H <sub>2</sub> uptake (mmol g <sup>-1</sup> )
	<i>T</i> <sub>p.m.</sub> <sup>a</sup> (°C)	H <sub>2</sub> -uptake (mmol g <sup>-1</sup> )	<i>T</i> <sub>p.m.</sub> (°C)	H <sub>2</sub> -uptake (mmol g <sup>-1</sup> )	<i>T</i> <sub>p.m.</sub> (°C)	H <sub>2</sub> -uptake (mmol g <sup>-1</sup> )	
Fresh	263	1.71	–	–	698	1.34	3.05
Used	289	0.69	415	0.25	698	1.55	2.49

<sup>a</sup> Temperature of peak maximum (°C).

Also, the H<sub>2</sub> consumption corresponding to the different reduction peaks is summarized in Table 3. If one assumes that the manganese ions in the LaMnO<sub>3</sub> catalyst were entirely Mn<sup>3+</sup> or Mn<sup>4+</sup> and completely reduced into Mn<sup>2+</sup>, the theoretical H<sub>2</sub> consumption would be 2.07 or 4.13 mmol g<sup>-1</sup>, respectively. With H<sub>2</sub>-TPR, however, the total H<sub>2</sub> consumption of the fresh and used LaMnO<sub>3</sub> catalysts was found to be 3.05 and 2.49 mmol g<sup>-1</sup>, respectively, confirming the cohabitation of Mn<sup>3+</sup> and Mn<sup>4+</sup> in both catalysts. Additionally, to assume that the reduction of Mn ions contributed to the total H<sub>2</sub> consumption, the oxygen stoichiometry in the perovskite can be quantitative determined based on the total H<sub>2</sub> consumption values. Stoichiometrical formulas of LaMnO<sub>3.23</sub> and LaMnO<sub>3.10</sub> were obtained for the fresh and used catalysts, respectively, which was in close accordance with the perovskite structures by XRD analysis in spite of the minor differences.

For the fresh and used catalysts, the H<sub>2</sub> uptake in the low-temperature range (below 500 °C) was 1.71 and 0.94 mmol g<sup>-1</sup>, respectively, whereas in the high-temperature range (above 500 °C) it was 1.34 and 1.55 mmol g<sup>-1</sup>, respectively. The lower low-temperature H<sub>2</sub> consumption of the used catalyst can be considered to be a key parameter affecting its catalytic performance in the reac-

tion, as it suggests weaker low-temperature reducibility, which in turn adversely affects the catalytic reactivity for VC oxidation. Furthermore, the low-temperature reducibility of the LaMnO<sub>3</sub> catalyst is closely related to the redox ability of the Mn<sup>4+</sup>/Mn<sup>3+</sup> couple. For the used catalyst, it can be deduced that the redox ability of Mn<sup>4+</sup>/Mn<sup>3+</sup> also weakened based on its lower H<sub>2</sub> uptake in the low-temperature range.

In addition, the chemical state and chemical surface composition of the fresh and used catalysts were determined by XPS (Table 4). For both catalysts, the surface molar ratios of La/Mn were higher than the nominal values (1.00) with 1.50 and 1.60 for the fresh and used catalysts, respectively. These results show that La enrichment occurred on the catalyst surface. It should be noted that the surface atomic ratio of carbon on the used catalyst was similar to that on the fresh catalyst, confirming the absence of coke formation on the catalyst surface and also in agreement with the TG/DTA results. Additionally, only a small amount of residual chlorine with an atomic ratio of 0.47% was detected on the used catalyst.

Fig. 9 shows the C 1s and Cl 2p XPS spectra of the fresh and used catalysts. On one hand, the C 1s spectra presented three peaks located at 284.8, 286.1 and 289.1 eV for both catalysts (Fig. 9A). The

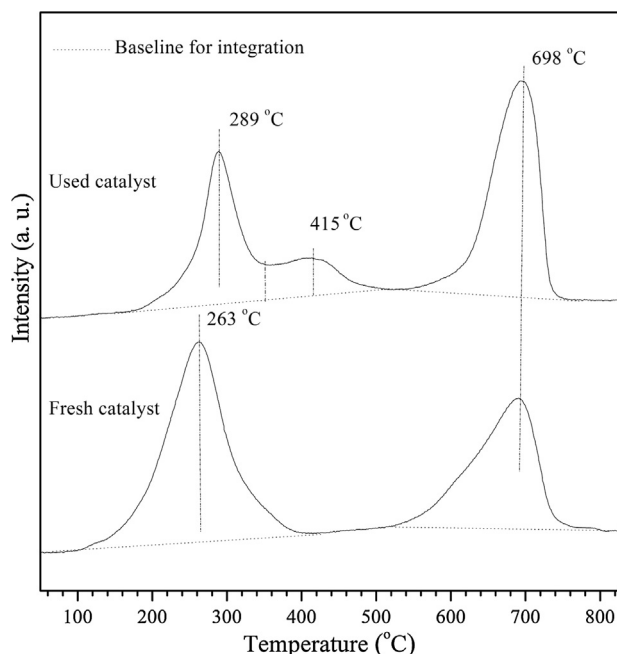


Fig. 8.  $H_2$ -TPR profiles of fresh and used catalysts.

Table 4

Binding energies and atomic ratios obtained from XPS analyses of fresh and used catalysts.

Elements	Binding energy (eV)	Atomic ratios (%)	
		Fresh	Used
La	–	15.01	17.47
Mn	–	10.07	10.94
Mn2p <sub>3/2</sub> (Mn <sup>3+</sup> )	641.5	–	–
Mn2p <sub>3/2</sub> (Mn <sup>4+</sup> )	642.9	–	–
O	–	47.09	44.82
O1s a	529.5	21.94	22.69
O1s b	530.7	5.37	6.44
O1s c	531.6	14.56	12.48
O1s d	533.3	5.22	3.21
C	–	27.83	26.30
Cl	–	0	0.47
Total	–	100.0	100.0
Molar ratios			
La/Mn	–	1.49	1.60
O <sub>ads</sub> /O <sub>latt</sub>	–	0.91	0.82

first peak could be attributed to the presence of adventitious carbon (C–H) [27,28], which is generally present on a solid surface due to atmospheric contamination. The second peak at 286.1 eV could be associated with C–C [29], suggesting the presence of some organic species on the surface. And finally, the third peak at 289.1 eV could be related to surface carbonate species [30,31], which could be yielded as a result of carbon–oxygen interaction during the thermal treatment.

On the other hand, the Cl 2p spectra (Fig. 9B) show a single peak at the low binding energy of 195.5 eV for the fresh catalyst, but three peaks at 195.5, 198.2 and 199.8 eV for the used catalyst. The first peak, present in both catalysts, could be associated with trivalent lanthanum ions [31]. This peak overlaps with the XPS spectrum corresponding to Cl 2p due to their similar binding energies. Meanwhile, the second and third peaks present only in the used catalyst could be associated with residual surface chlorine species and with chemically-bonded chlorine in adsorbed chlorinated organic species, respectively [32,33]. These results verify the presence of surface chlorine species on the used catalyst, which

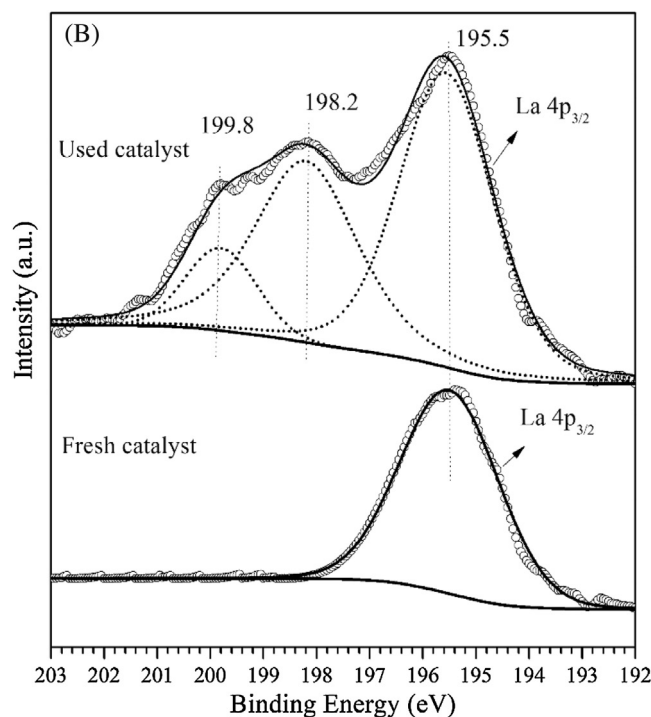
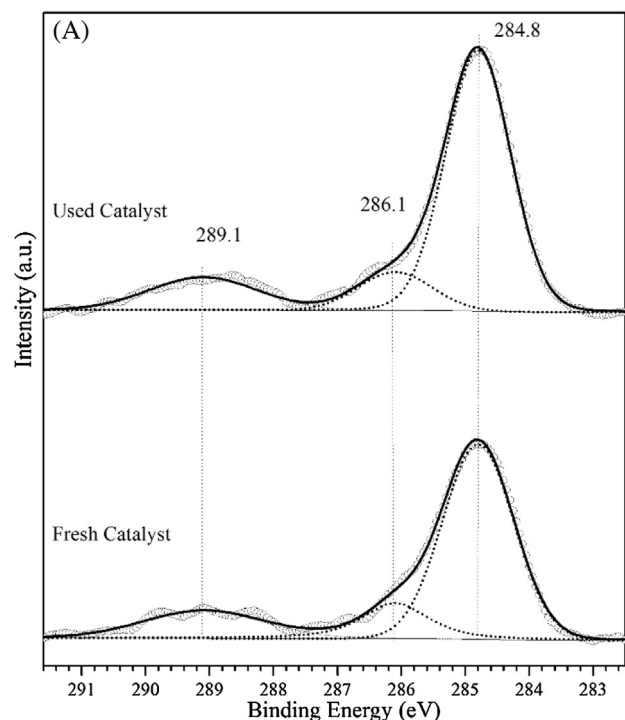


Fig. 9. (A) C 1s and (B) Cl 2p XPS spectra of fresh and used catalysts.

is consistent with the results of surface adsorbates analysis in the thermal treatment and chlorine content in Table 4.

The Mn 2p<sub>3/2</sub> and Mn 3s XPS spectra of the fresh and used catalysts are shown in Fig. 10. Both catalysts presented an asymmetrical signal at 642.0 eV attributable to Mn 2p<sub>3/2</sub> (Fig. 10A). According to the evidence about the coexistence of Mn<sup>4+</sup> and Mn<sup>3+</sup> ions in LaMnO<sub>3</sub> catalysts reported in [34,35], the spectra can be decomposed into two main peaks at binding energies of 641.5 and 642.9 eV assignable to Mn<sup>3+</sup> and Mn<sup>4+</sup> ions, respectively [35,36].

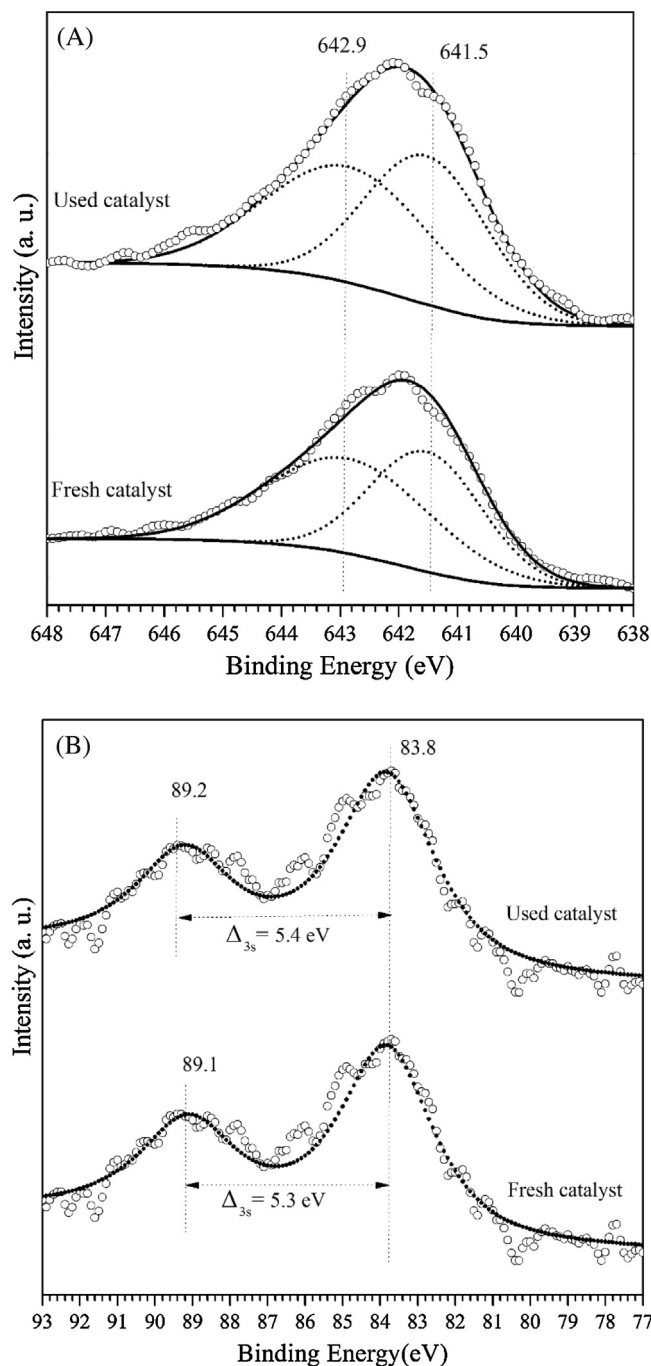


Fig. 10. (A) Mn 2p<sub>3/2</sub> and (B) Mn 3s XPS spectra of fresh and used catalysts.

Considering that the binding energies of Mn<sup>3+</sup> and Mn<sup>4+</sup> did not differ substantially in the Mn 2p<sub>3/2</sub> spectra, the approach of Galakhov et al. [37] was applied to the Mn 3s energy region in order to elucidate the average oxidation states of manganese ions on fresh and used catalysts. As indicated in Fig. 10B, the splitting values ( $\Delta E_{3s}$ ) of fresh and used catalysts were 5.3 and 5.4 eV, respectively. Moreover, the Mn 3s spectra of MnO, Mn<sub>3</sub>O<sub>4</sub>, Mn<sub>2</sub>O<sub>3</sub> and MnO<sub>2</sub> as reference oxides were recorded, and their splitting values were quantitatively measured (shown in Fig. S2). As shown in Fig. 11, the Mn 3s spectrum of MnO<sub>2</sub> exhibited the lowest splitting value, while the magnitude of the splitting from MnO<sub>2</sub> to MnO increased linearly. Accordingly, a linear relationship was obtained between the formal oxidation state of Mn and the splitting values ( $\Delta E_{3s}$ ) of Mn 3s spectra. A linear fitting calculation showed

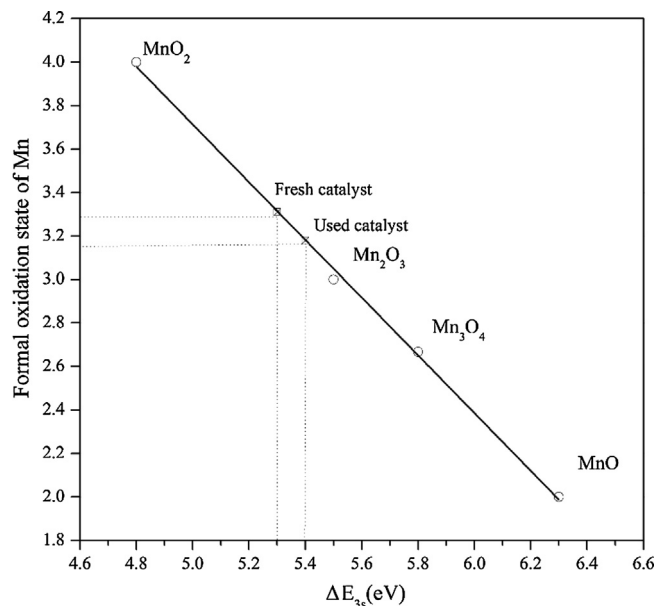


Fig. 11. Relationship between formal oxidation state of Mn and splitting values ( $\Delta E_{3s}$ ) of Mn 3s spectra.

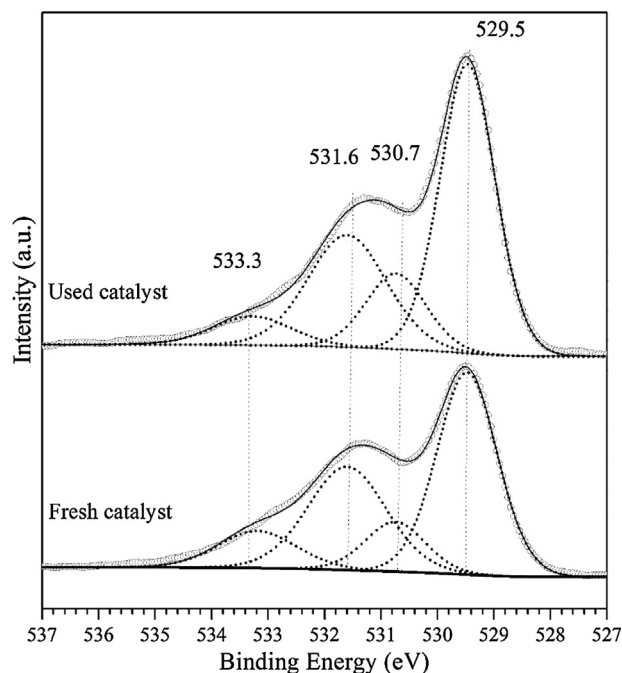


Fig. 12. O 1s spectra of fresh and used catalysts.

the  $\Delta E_{3s}$  values of the formal oxidation states of manganese for the fresh and used catalysts to be +3.31 and +3.18, corresponding to the chemical formulas of La(Mn<sup>4+</sup><sub>0.31</sub>)(Mn<sup>3+</sup><sub>0.69</sub>)O<sub>3.16</sub> and La(Mn<sup>4+</sup><sub>0.18</sub>)(Mn<sup>3+</sup><sub>0.82</sub>)O<sub>3.09</sub>, respectively. The coexistence of Mn<sup>4+</sup> and Mn<sup>3+</sup> in the catalysts is therefore confirmed by H<sub>2</sub>-TPR analysis and the Mn 2p<sub>3/2</sub> spectra. Additionally, the formal oxidation state of Mn for the used catalyst was lower than for its fresh counterpart, indicating a decrease in surface Mn<sup>4+</sup> concentration.

The O 1s XPS spectra of the fresh and used catalysts are illustrated in Fig. 12. A curve fitting method was used to identify four components, namely O 1s a, O 1s b, O 1s c and O 1s d, at the respective binding energies of 529.5, 530.7, 531.6 and 533.3 eV (Table 4). The most intense peak at the lowest binding energy (529.5 eV) was assigned to lattice oxygen (O<sub>latt</sub>: O<sup>2-</sup>), while the peak at the high-



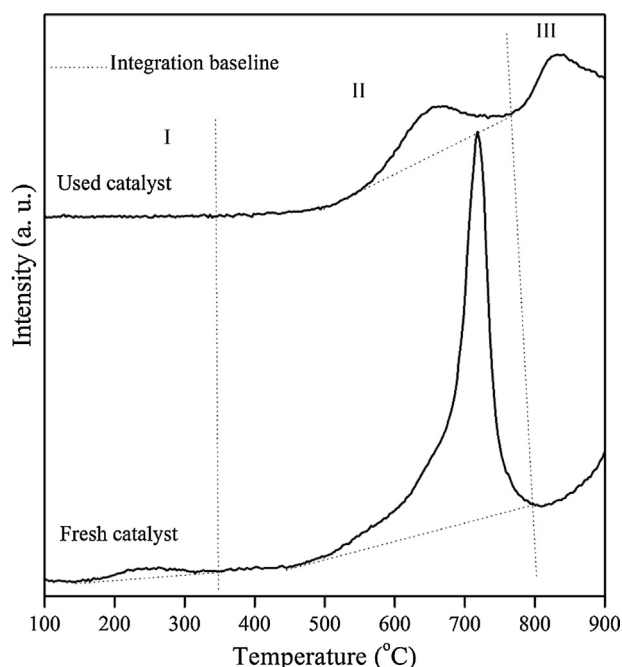
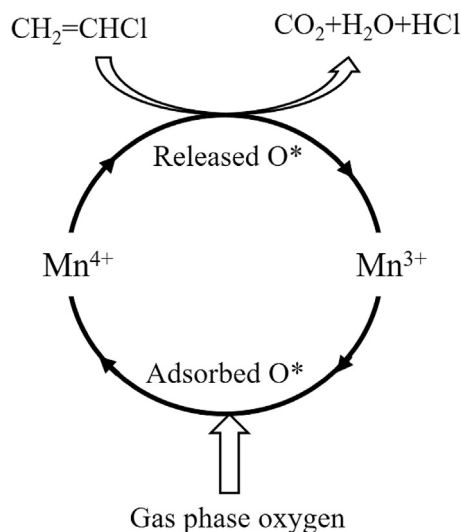


Fig. 13.  $O_2$ -TPD profiles of fresh and used catalysts.

est binding energy (533.3 eV) was attributed to adsorbed molecular water [38]. The two peaks at the intermediate binding energies could be attributed to surface adsorbed oxygen species ( $O_{ads}$ ). The first one at 530.7 eV corresponds to adsorbed oxygen ( $O^-/O_2^{2-}$ ), and the second one at 531.6 eV can be assigned to oxygen-containing groups such as hydroxyl ( $OH^-$ ) and/or carbonate ( $CO_3^{2-}$ ) in the form of surface adsorbates [39,40].

Moreover, the molar ratio of surface adsorbed oxygen species versus lattice oxygen ( $O_{ads}/O_{lat}$ ) was evaluated in order to quantify the amount of active species on the surface of the catalysts (Table 4). The used catalyst displayed a lower molar ratio than the fresh one, indicating a decrease in the abundance of  $O_{ads}$  species. The smaller amounts of surface adsorbed oxygen after the catalytic reaction of VC oxidation could therefore be responsible for the deactivation of  $LaMnO_3$  catalyst, as demonstrated previously [18,19].

In order to verify the influence of surface and bulk oxygen species on deactivation,  $O_2$ -TPD measurements were performed over fresh and used catalysts. Fig. 13 shows the oxygen desorption profiles within the temperature range of 100–900 °C, with three oxygen desorption regions (denoted I, II and III) observed for both catalysts. Region I presented a broad desorption peak for the fresh catalyst, but a negligible desorption signal for the used one. According to the literature [41,42], the desorbed oxygen in this region could be ascribed to the weakest molecular physisorbed and/or chemisorbed oxygen on the catalyst surface. Region II showed that larger amounts of oxygen originating from surface over-stoichiometric oxygen and subsurface oxygen via oxygen vacancies were gradually desorbed as the temperature increased [43]. For the fresh catalyst, a wide, intense peak centered at 720 °C was observed, indicating its rapid oxygen migration and desorption behaviors. In contrast, the weak peak intensity over the used catalyst suggested its lower desorption rate of oxygen species in this region. At higher temperature, the desorbed oxygen in region III could be related to the crystal lattice of the perovskite structure. Moreover, different desorption behaviors of lattice oxygen were observed for the fresh and used catalysts. For the fresh catalyst, the desorption signal started above 800 °C and was uncompleted till 900 °C, while the desorption of lattice oxygen progressed easily and successfully



Scheme 1. Reaction mechanism for VC oxidation in  $Mn^{4+}/Mn^{3+}$  redox cycle.

with the presence of a small peak between 800 and 900 °C over the used catalyst.

Moreover, the amount of desorbed oxygen per weight of catalyst was quantified for regions I and II. The fresh and used catalysts presented desorption values of 0.0103 and 0.0019 mmol  $g^{-1}$  in region I, and 0.2276 and 0.1021 mmol  $g^{-1}$  in region II, respectively.

Based on these results, it can be concluded that the diminished activity of the used catalyst was due to (i) the lower concentration of adsorbed oxygen resulting from its decreased SSA and (ii) the smaller amounts of over-stoichiometric oxygen resulting from its lower surface  $Mn^{4+}$  concentration and formal oxidation state of manganese, accordingly leading to less oxygen vacancies generation and inhibited surface oxygen mobility in the reaction.

### 3.3. Discussion and reaction mechanism

The aforementioned characterizations and catalytic testing results are useful for examining the influence of the physicochemical properties on catalytic deactivation. It has been reported that the main parameters resulting in the evident deactivation of CVOs oxidation catalysts are those including the presence of coke deposition, the attack enacted by concentrated Cl species and the decrease in SSA, reducibility and oxygen mobility. Based on TG/DTA and adsorbates analysis, coke formation was undetected on the used catalyst, which seems to exclude the possibility of deactivation by coking. Traces of Cl species on the surface of the used catalyst (atomic ratio of 0.47%) were, however, observed by XPS analysis. Also, no structural transformation was observed for the used  $LaMnO_3$  perovskite oxide.

Nevertheless, obvious differences in SSA, low-temperature reducibility, formal oxidation state of Mn, surface oxygen capacity and mobility were observed from the characterizations results of BET,  $H_2$ -TPR, XPS and  $O_2$ -TPD, which indicated that these were the main parameters responsible for catalytic deactivation. Indeed, the used catalyst exhibited lower SSA and low-temperature reducibility as well as smaller amounts of surface oxygen species in comparison with the fresh one. In addition, the  $H_2$  consumption in the low-temperature region and the total amounts of desorbed oxygen from surface and subsurface (regions I and II in  $O_2$ -TPD profiles) were greatly affected by the SSA, indicating a close internal relationship among these properties. Moreover, the used catalyst showed a lower formal oxidation state of Mn and weakened surface oxygen mobility at low temperature.

Thus, considering the relationship between these properties and the redox ability of the  $\text{Mn}^{4+}/\text{Mn}^{3+}$  couple, a plausible reaction mechanism was proposed on the basis of the redox cycle between  $\text{Mn}^{4+}$  and  $\text{Mn}^{3+}$  ions in the  $\text{LaMnO}_3$  perovskite oxide (Scheme 1). On one hand, VC molecules react with released  $\text{O}^*$  ( $\text{O}^*$  denotes activated oxygen species) on the surface, which results in the production of  $\text{CO}_2$ ,  $\text{H}_2\text{O}$  and  $\text{HCl}$ . In this process, the release of  $\text{O}^*$  can be formulated as  $2\text{Mn}^{4+} + \text{O}^{2-} \rightarrow 2\text{Mn}^{3+}[\text{Vo}] + \text{O}^*$ , in which the migration and activation of surface oxygen are implemented via oxygen vacancies ( $[\text{Vo}]$ ) in the perovskite. On the other hand, oxygen from the gas phase can be activated by oxygen vacancies simultaneously with the oxidation of  $\text{Mn}^{3+}$  into  $\text{Mn}^{4+}$ . The poorer catalytic activity presented by the used catalyst could thus be attributed to inhibited redox behavior in this proposed cycle: (i) lower amounts of surface  $\text{Mn}^{4+}$  on the used catalyst reduce the formation of oxygen vacancies, decreasing the amount of released active oxygen species, thereby hindering VC oxidation; and (ii) lower amounts of surface oxygen vacancies weaken the activation ability of gas phase oxygen, also hindering VC oxidation.

In addition, as a result of the gradual decrease in the oxidation activity of the  $\text{LaMnO}_3$  catalyst, VC could not be completely destructed at  $350^\circ\text{C}$ . Accordingly, the chlorine species on the catalyst surface, through being strongly activated due to the catalytic effect of  $\text{LaMnO}_3$ , prompted a series of chlorination reactions with VC molecules, leading to the formation of various higher chlorinated hydrocarbons. Previous study has been reported that the active chlorine species could therefore promote secondary chlorination reactions and favor the formation of chlorinated organic species [44]. Additionally, the initial chlorohydrocarbon, i.e.,  $\text{CHCl}_2\text{CH}_2\text{Cl}$ , could not be oxidized due to a lack of active oxygen species on the catalyst surface, but was thermally decomposed into cracking intermediates, which in turn formed small chlorinated compounds through reaction with chlorine. This confirms that catalytic deactivation of  $\text{LaMnO}_3$  catalyst results in the formation of various chlorinated organics by-products, which cannot be fully oxidized.

#### 4. Conclusions

The catalytic stability and durability of  $\text{LaMnO}_3$  perovskite oxide prepared by conventional co-precipitation were assessed for the catalytic oxidation of vinyl chloride, and the relationship between catalytic deactivation and the physicochemical properties of the fresh and used catalysts was evaluated.

In this study,  $\text{LaMnO}_3$  perovskite oxide exhibited poor catalytic stability and durability during the process of VC oxidation, with a gradual decrease in activity during four consecutive light-off catalytic runs and a steady-state experiment (120 h at  $350^\circ\text{C}$ ). Additionally, the deactivation of  $\text{LaMnO}_3$  perovskite oxide was irreversible without any observation of catalytic regeneration after an oxidative treatment. Considerable amounts of chlorinated organic by-products ( $\text{CHCl}_3$ ,  $\text{CCl}_4$  and  $\text{CHCl}_2\text{CH}_2\text{Cl}$ ) were detected in the reaction, which could be related to the presence of Cl species and the catalytic deactivation of  $\text{LaMnO}_3$  perovskite oxide.

According to the characterization results for the fresh and used catalysts, the used catalyst remained a perovskite structure without any other phases, but lattice expansion and enlarged crystallite size were observed. No coke formation but only trace amounts of residual Cl species were detected on the used catalyst, indicating that coking and chlorine attack were not the main reasons for deactivation. Nonetheless, the used catalyst presented lower specific surface area, weakened low-temperature reducibility, lower  $\text{Mn}^{4+}/\text{Mn}^{3+}$  molar ratio and inhibited surface oxygen mobility compared to its fresh counterpart. These parameters were therefore considered to be the ones principally responsible for deactivation. Finally, a deactivation mechanism was proposed based on the redox

cycle of the  $\text{Mn}^{4+}/\text{Mn}^{3+}$  couple, with the redox ability of  $\text{Mn}^{4+}/\text{Mn}^{3+}$  and oxygen vacancies playing significant roles in VC oxidation.

#### Acknowledgments

This research was financially supported by National Basic Research Program of China (2013CB933200), National Natural Science Foundation of China (21577035), Commission of Science and Technology of Shanghai Municipality (15DZ1205305) and 111 Project (B08021). The authors would like to acknowledge the China Scholarship Council for the Joint-Training Scholarship Program with Institut de Recherches sur la Catalyse et l'Environnement de Lyon (IRCELYON) of Université Claude Bernard Lyon 1 (UCBL1).

#### Appendix A. Supplementary data

Supplementary data associated with this article can be found, in the online version, at <http://dx.doi.org/10.1016/j.apcatb.2015.12.052>.

#### References

- [1] Thematic Strategy on Air Pollution, Communication from the Commission to the Council and The European Parliament, Commission of the European Communities, COM (2005) 446 final, Brussels, 2005.
- [2] Protocol to the 1979 Convention on Long-range Trans-Boundary Air Pollution to the Abate Acidification, Eutrophication and Ground-Level Ozone, United Nations, 2000.
- [3] S. Pitkäaho, L. Matejova, K. Jiratova, S. Ojala, R.L. Keiski, Appl. Catal. B 126 (2012) 215–224.
- [4] I. Maupin, L. Pinard, J. Mijoin, P. Magnoux, J. Catal. 291 (2012) 104–109.
- [5] E. Finocchio, G. Sapienza, M. Baldi, G. Busca, Appl. Catal. B 51 (2004) 143–148.
- [6] R. López-Fonseca, J.I. Gutiérrez-Ortiz, M.A. Gutiérrez-Ortiz, J.R. González-Velasco, J. Catal. 209 (2002) 145–150.
- [7] Q. Dai, H. Huang, Y. Zhu, W. Deng, S. Bai, X. Wang, G. Lu, Appl. Catal. B 117–118 (2012) 360–368.
- [8] B. de Rivas, R. López-Fonseca, C. Jiménez-González, J.I. Gutiérrez-Ortiz, J. Catal. 281 (2011) 88–97.
- [9] J.R. González-Velasco, R. López-Fonseca, A. Aranzabal, J.I. Gutiérrez-Ortiz, P. Steltenpohl, Appl. Catal. B 24 (2000) 233–242.
- [10] S. Chatterjee, H.L. Greene, Y. Joon Park, Catal. Today 11 (1992) 569–596.
- [11] A. Aranzabal, M. Romero-Sáez, U. Elizundia, J.R. González-Velasco, J.A. González-Marcos, J. Catal. 296 (2012) 165–174.
- [12] Y. Dai, X. Wang, Q. Dai, D. Li, Appl. Catal. B 111–112 (2012) 141–149.
- [13] B. de Rivas, N. Guillén-Hurtado, R. López-Fonseca, F. Coloma-Pascual, A. García-García, J.I. Gutiérrez-Ortiz, A. Bueno-López, Appl. Catal. B 121–122 (2012) 162–170.
- [14] D. Kießling, R. Schneider, P. Kraak, M. Haftendorn, G. Wendt, Appl. Catal. B 19 (1998) 143–151.
- [15] R. Schneider, D. Kiessling, R. Herzschuh, G. Wendt, React. Kinet. Catal. Lett. 61 (1997) 245–250.
- [16] G. Sinquin, J.P. Hindermann, C. Petit, A. Kiennemann, Catal. Today 54 (1999) 107–118.
- [17] G. Sinquin, C. Petit, S. Libs, J.P. Hindermann, A. Kiennemann, Appl. Catal. B 32 (2001) 37–47.
- [18] C. Zhang, C. Wang, W. Zhan, Y. Guo, Y. Guo, G. Lu, A. Baylet, A. Giroir-Fendler, Appl. Catal. B 129 (2013) 509–516.
- [19] C. Zhang, C. Hua, C. Wang, Y. Guo, Y. Guo, A. Baylet, A. Giroir-Fendler, Appl. Catal. B 134–135 (2013) 310–315.
- [20] J.A. Alonso, M.J. Martínez-Lope, M.T. Casais, J.L. MacManus-Driscoll, P.S.I.P.N. de Silva, L.F. Cohen, M.T. Fernández-díaz, J. Mater. Chem. 7 (1997) 2139–2144.
- [21] B. He, Q. Song, Q. Yao, Z. Meng, C. Chen, Korean J. Chem. Eng. 24 (2007) 503–507.
- [22] R. Delaigle, P. Eloy, E.M. Gaigneaux, Catal. Today 192 (2012) 2–9.
- [23] H. Li, G. Lu, Q. Dai, Y. Wang, Y. Guo, Y. Guo, Appl. Catal. B 102 (2001) 475–483.
- [24] A. Aranzabal, J.A. González-Marcos, M. Romero-Sáez, J.R. González-Velasco, M. Guillemot, P. Magnoux, Appl. Catal. B 88 (2009) 533–541.
- [25] A. Baylet, S. Royer, C. Labrugère, H. Valencia, P. Marécot, J.M. Tatibouët, D. Duprez, Phys. Chem. Chem. Phys. 10 (2008) 5983–5992.
- [26] L. Lisi, G. Bagnasco, P. Ciambelli, S. De Rossi, P. Porta, G. Russo, M. Turco, J. Solid State Chem. 146 (1999) 176–183.
- [27] A. Yan, V. Maragou, A. Arico, M. Cheng, P. Tsiakaras, Appl. Catal. B 76 (2007) 320–327.
- [28] S.M. Lima, J.M. Assaf, M.A. Peña, J.L.G. Fierro, Appl. Catal. A 311 (2006) 94–104.
- [29] J.-M. Giraudon, A. Elhachimi, F. Wyrwalski, S. Siffert, A. Aboukaïs, J.-F. Lamonier, G. Leclercq, Appl. Catal. B 75 (2007) 157–166.
- [30] N.H. Batis, P. Delichereb, H. Batis, Appl. Catal. A 282 (2005) 173–180.
- [31] D.D. Sarma, C.N.R. Rao, J. Electron Spectrosc. Relat. Phenom. 20 (1980) 25–45.

- [32] X. Wang, C. Wang, W. Jiang, W. Guo, J. Wang, *Chem. Eng. J.* 189–190 (2012) 288–294.
- [33] T.G. Vargo, J.A. Gardella, *J. Vac. Sci. Technol. A* 7 (1989) 1733–1741.
- [34] M. Alifanti, J. Kirchnerova, B. Delmon, *Appl. Catal. A* 245 (2003) 231–243.
- [35] J.C. Carver, G.K. Schweitzer, T.A. Carlson, *J. Chem. Phys.* 57 (1972) 973–981.
- [36] S. Ponce, M.A. Peña, J.L.G. Fierro, *Appl. Catal. B* 24 (2000) 193–205.
- [37] V.R. Galakhov, *Phys. Rev. B* 65 (2002) 113102.
- [38] H. Najjar, J.-F. Lamonier, O. Mentré, J.-M. Giraudon, H. Batis, *Appl. Catal. B* 106 (2011) 149–159.
- [39] H. Liang, Y. Hong, C. Zhu, S. Li, Y. Chen, Z. Liu, D. Ye, *Catal. Today* 201 (2013) 98–102.
- [40] N.A. Merino, B.P. Barbero, P. Eloy, L.E. Cadús, *Appl. Surf. Sci.* 253 (2006) 1489–1493.
- [41] S. Liang, T. Xu, F. Teng, R. Zong, Y. Zhu, *Appl. Catal. B* 96 (2010) 267–275.
- [42] H. Zhang, Y. Shimizu, Y. Teraoka, N. Miura, N. Yamazoe, *J. Catal.* 121 (1990) 432–440.
- [43] H. Najjar, J.F. Lamonier, O. Mentré, J.M. Giraudon, H. Batis, *Appl. Catal. B* 106 (2011) 149–159.
- [44] A. Aranzabal, M. Romero-Sáez, U. Elizundia, J.R. González-Velasco, J.A. González-Marcos, *J. Chem. Technol. Biotechnol.* (2014), <http://dx.doi.org/10.1002/jctb.4585>.